INSTRUMENTATION AND CALCULATIONS FOR MATTER-WAVE

INTERFEROMETRY EXPERIMENTS

by

Daniel J. Christensen

A senior thesis submitted to the faculty of

Brigham Young University

in partial fulfillment of the requirements for the degree of

Bachelor of Science

Department of Physics and Astronomy

Brigham Young University

August 2007

BRIGHAM YOUNG UNIVERSITY

DEPARTMENT APPROVAL

of a senior thesis submitted by

Daniel J. Christensen

This thesis has been reviewed by the research advisor, research coordinator, and department chair and has been found to be satisfactory.

_____   _____
Date   Dallin Durfee, Advisor

_____   _____
Date   Eric Hintz, Research Coordinator

_____   _____
Date   Ross Spencer, Chair

ABSTRACT

INSTRUMENTATION AND CALCULATIONS FOR MATTER-WAVE

INTERFEROMETRY EXPERIMENTS

Daniel J. Christensen

Department of Physics and Astronomy

Bachelor of Science

This thesis presents two projects connected by a similar element of atom interferometry. First I describe the development of a stable and high-flux thermal atom-beam source to be used in an improved atomic time standard. Preliminary measurements have shown that this source produces an atomic beam with a flux $\geq 3.422 \times 10^{12}$ atoms per second with a most probable velocity of 750m/s. Then I present calculations verifying the feasibility of a proposed ion interferometer capable of setting a new lower limit on the mass of a photon. Our group's initial model assumed an ion interferometer inside an infinite cylinder with no fringing fields. The calculations I present show that the infinite cylinder assumption is a viable approximation and that the classical fringing fields are negligible.

ACKNOWLEDGMENTS

There will probably not be too many times in my life when I will enter a project having virtually no experience with the material or knowledge of appropriate professional technique. I thank my advisor Dr. Dallin Durfee not only for his expertise and mentoring as a physicist, but also for his example and genuine care and concern as a person. I feel that I have been afforded many opportunities and learning experiences well beyond the usual course of education due to my association with him and his research group. I also thank the students who have worked with me, taught me, and assisted me — mainly Justin Paul, Brian Neyenhuis, Chris Erickson, and Greg Doermann. As an experimentalist, I would be lost with out our machinist Wes Lifferth. His expertise and input literally helped shape many of the apparatuses presented in this thesis. It is also appropriate for me to acknowledge John Ellsworth and Scott Daniels for their electronics and materials expertise, as well as Dr. Ross Spencer for his assistance with computational methods. I must also express my sincere appreciation for my wife Lisa, as her diligent work ethic has been a model for me and has inspired me to do my absolute best academically. She has also been a wonderful support to me both as a mother to our child and as a wife to me throughout this entire research experience.

Contents

List of Figures

Chapter 1

Introduction

Our research group is currently building a highly precise and stable atom interferometer/atomic time standard. This is an atomic clock which, among other capabilities, will enable precision measurements of fundamental constants. Some of the long term goals of this project include time rate-of-change measurements of the fine structure constant, measurements of time dilation, and inertial force sensors.

An interferometer can be described as a precision measurement instrument relying on the interference of waves. In our experiment, we are interfering calcium atoms in different atomic states. The "timing mechanism" of the clock is generated by carefully measuring the energy states of the atoms after they interact with the lasers.

This senior thesis describes two separate projects connected by the similar element of atom interferometry. Chapter two presents the development of a thermal atomic beam source which will be utilized in the previously mentioned atomic time standard.

While working on this project, some members of our group thought of a novel application of interferometers which would set a new lower limit on the mass of a photon. Chapter three describes calculations which I performed to confirm the validity of this proposed table-top experimental apparatus.

Chapter 2

Atomic Beam Characterization and Manipulation

2.1 Background and motivation

Our interferometer will utilize a thermal beam of calcium atoms. We chose a thermal beam over other common sources (such as atom traps and the fountain design) because a thermal beam is more simple, robust, and cost effective and provides a high flux of atoms.

Simply stated, a thermal atomic beam is created by heating a substance in a vessel which has a hole in it for the substance to escape. Specifically for the calcium beam, we will be heating it in a crucible placed in an oven. Regardless of temperature, the calcium will always have a certain amount of its own vapor around it. As the calcium heats up, the vapor becomes more dense and a higher percentage of the vapor effuses from the source. By heating the calcium in vacuum, the mean free path of the atoms is large and a beam is formed.

It is important to note the relationship of pressure and velocity with respect to
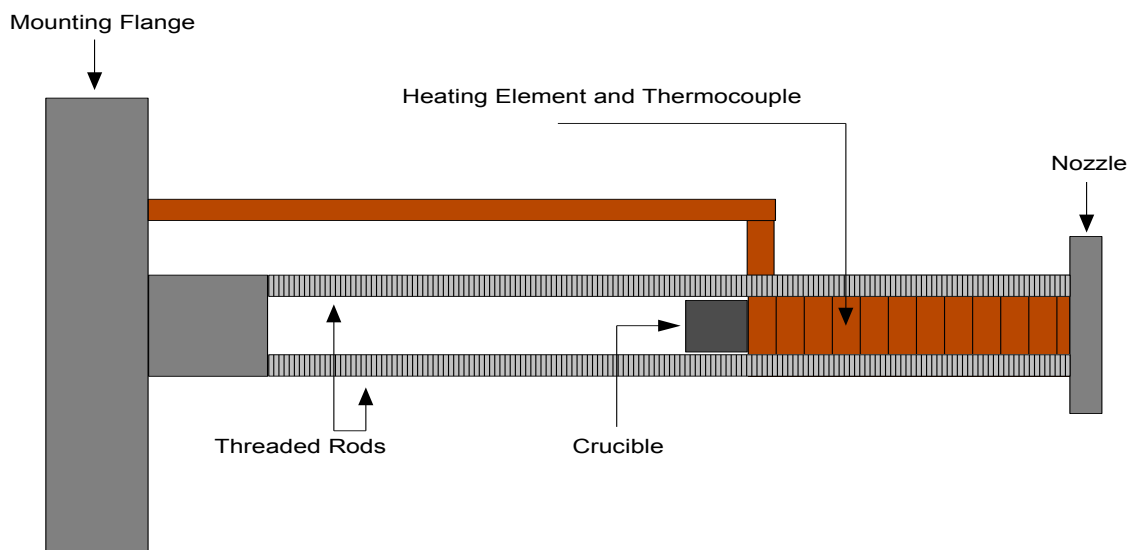
3

Figure 2.1 Old Oven Configuration

temperature in calcium atoms. As temperature rises, calcium's vapor pressure rises much faster than it's velocity. Therefore as we raise the temperature of the calcium, a more dense beam is formed while the atoms' velocity remains comparably stable. This correlates to a higher flux of atoms in the beam — which is what we want. For this reason we will heat the oven as hot as possible for the experiment.

2.2 Development and Characterization of a Thermal Atomic Beam Source

2.2.1 Development of an Oven

Generally, an oven consists of a container which holds the substance to be heated and a device to heat that substance. The container only needs to have a way to be loaded and an opening through which the heated substance can exit. We are using a stainless steel cylindrical crucible with a cap on one end and a hole in the other.

We had originally been given a simple oven from another research group (see Fig. 2.1), but knew nothing about its performance. The oven consisted of a heating coil mounted among 4 threaded rods, which were in turn mounted directly to a flange. The crucible, as the only movable part of the system, had to be loaded between the rods, through the backside of the coils. The crucible was held in place only by gravity and the front nozzle. All wires, including a thermocouple, were integrated into the heating coil, and exited out the backside of the flange. The entire length of the device, from flange to nozzle, was covered by a thin, removable, cylindrical tube (not pictured) which served as a heat shield. We used standard digital temperature controllers to deliver current to the coils.

This oven exhibited many flaws and ultimately served as a learning tool which helped me design a second-generation oven. The crucible was made entirely of stainless steel, an inefficient thermal conductor which allowed the possibility of significant thermal gradients.

The crucible also fit poorly into the heating coils. Since the crucible was held in the coils only by gravity and the front nozzle, there was virtually no way to assure consistent alignment of the crucible from one test to another. Furthermore, the coils were becoming deformed through many uses and made poor physical contact with the crucible. We tried to salvage this oven by making a new crucible out of copper (thermal conductivity about $28\frac{1}{2}$ times that of stainless steel) with a stainless steel insert (see Fig. 2.2), but we still did not observe a flux of atoms acceptable for our experiment.

By attaching a thermocouple to the crucible, we also determined that the coils were not heating the crucible nearly as hot as we had expected. Additionally we observed that calcium was building up and condensing in the rear of the crucible, indicating that the front of the device was hotter than the back while in its steady-
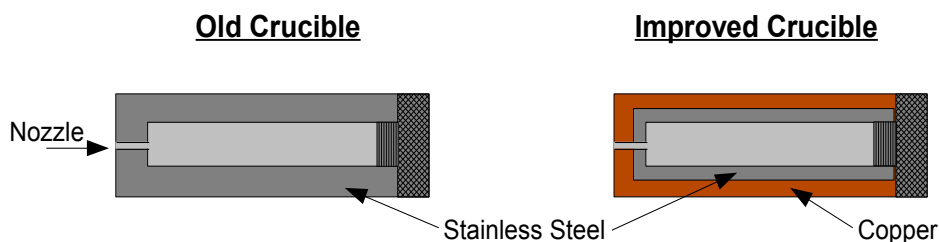
Figure 2.2 Cutaways of the original and improved crucible designs. The original crucible was made entirely of stainless steel, while the improved crucible was made of copper with a pressure fit stainless steel insert.

state. We arrived at the same result even with the new crucible.

New Oven Design

I designed a source which outputs a stable and high-flux beam of atoms (see Fig. 2.3) that also corrects all the previously mentioned problems of the original oven. The device uses external, removable band heaters that allow for more simple and measurable heating of the oven. Two tubes positioned in a crossing "X" shape at the mouth of the oven allow the experimenter to optically probe and transversely laser cool the atomic beam very close to the source. The crucible was designed to fit snugly in the oven for maximum thermal conductivity, and has a positioning system that assures consistent alignment from one test run to another.

The source consists of three main sections and the crucible, all made of stainless steel because of its vacuum compatibility and non-reactance with calcium. There is a thick copper sleeve (long enough to accommodate two band heaters) around the back end of the apparatus. Again, copper is used here to improve thermal conductivity. The crucible (not pictured) is located inside. The band heaters (also not pictured) are powered by standard digital temperature controllers.

Welded to this section are four stainless steel cylindrical tubes. They will allow
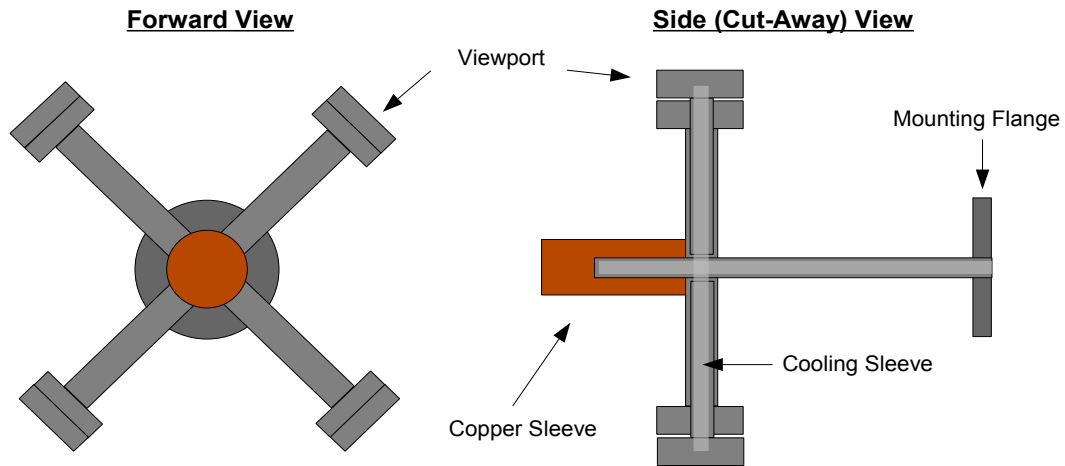
Figure 2.3 New Atom-Beam Source Configuration. The oven (rear section) is covered by a copper sleeve and is where the band heaters (not pictured) will attach. The tubes crossing in an "X" give visual access to the atomic beam immediately after the oven. This section is connected by a long tube to a flange which mounts directly to the experiment chamber.

lasers to transversely cool the atoms immediately after they leave the oven. Capping each tube is a conflat viewport. Inside (and coaxial with) each tube is another tube of slightly smaller diameter. Because these inner "sleeves" are connected only at the top of each tube, they provide a cold wall to which stray atoms can attach so that the viewports stay clear. Otherwise, because of the walls' close proximity to the oven, they will be hot enough to transmit stray atoms to the viewports and "fog" them up.

The final section welded to the apparatus is a long, thin stainless steel tube leading to a connecting flange. I designed the tube to be long and thin so that minimal heat would be conducted to the rest of the experimental setup. Though thin and long, I was still careful to make the tube rigid enough to support the structure and short enough that the atom-beam would be adequately dense.

The crucible is constructed of thin stainless steel, and is designed to fit snugly inside of the oven. It is attached to a long rod (see Fig. 2.4) so that it can be
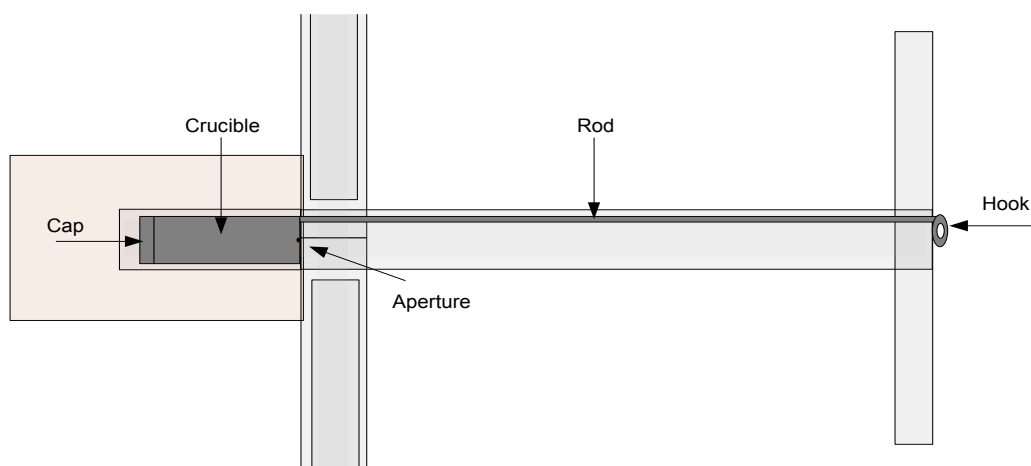
Figure 2.4 New crucible design shown inside of the new oven. The crucible is lowered in place by a long rod and held in position by a hook which attaches to a set screw (not pictured) on the flange.

lowered into the oven via the opening in the flange. On the end of the rod is a hook which attaches to a screw on the inside of the flange. This positioning system assures consistent axial and radial alignment from one test run to another.

2.2.2   Characterization of the Beam with Optical Absorption

To characterize the atomic beam produced by the source, I employed a well-known light absorption technique. The setup is rather simple (see Fig. 2.5). I sent a laser beam through the atoms and measured what percent of the laser's intensity was lost due to absorption into the atomic beam.

Using a well-established relationship between percent absorption and the qualities of an absorptive material (Beer's law), the flux of the atom-beam can be determined. Assuming a laser wavelength of 423nm. and an oven temperature of 680° Celsius, we would expect to observe about 10% absorption of the light.
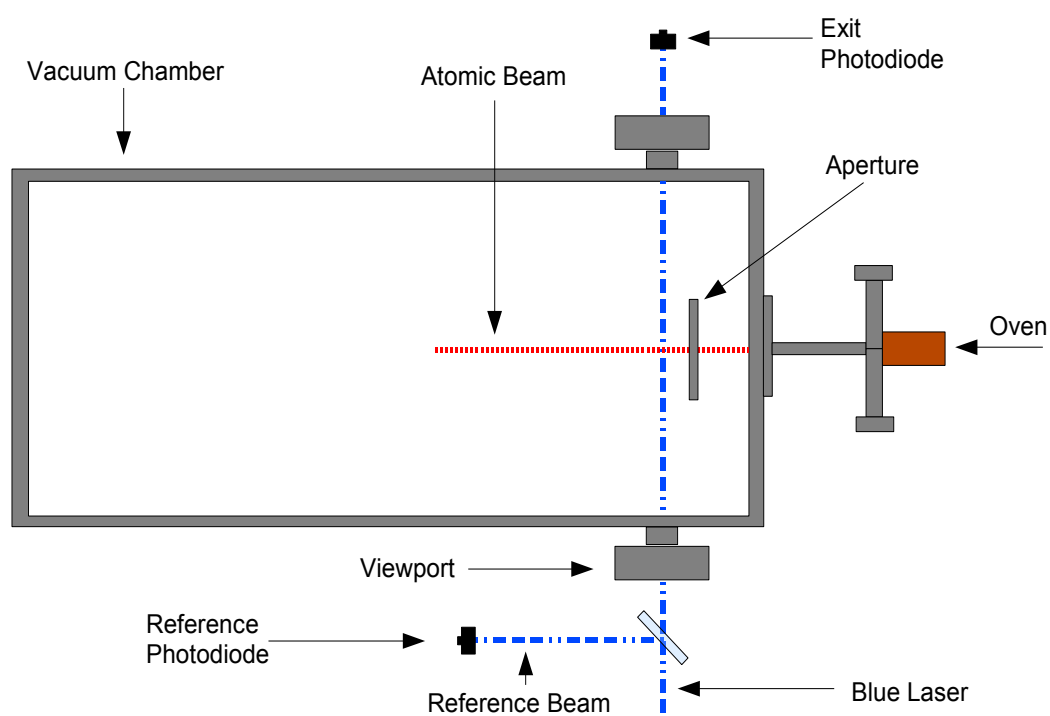
Figure 2.5 "Bird's Eye View" of the Experimental Setup

I used blue laser to probe the $^1S_0(4s^2)$ transition in calcium and determined the absorption of the laser into the atomic beam by measuring the laser's exiting intensity. To account for fluctuations in the laser beam itself, I measured the absorption by comparing the intensity of the laser entering the system with the intensity of the laser exiting the system. As seen in Fig. 2.5, I picked off a portion of the blue laser before it entered the chamber and directed it to a photodiode, labeled "Reference Photodiode" in Fig. 2.5. I then fed the beam that had passed through the atoms into a second photodiode, labeled "Exit Photodiode" in Fig. 2.5, and compared the ratio of their intensities on an oscilloscope.

Because the frequency of the blue laser naturally drifts, I had to ramp the frequency of the laser while taking measurements. This assured that I was measuring absorption at the exact transition frequency. To do this, I used a reference calcium cell so I could see when the laser was on resonance, and a function generator to ramp the frequency of the laser.

With the newly designed source, measurements taken while ramping the frequency of the laser showed approximately 7.5% of the laser light being absorbed into the atomic beam. Beer's law states that $T_r = e^{-\sigma nt}$, where T_r is the percent of light transmitted, σ is the absorption cross section of the calcium atoms, n is the density of the atomic beam, and t is the beam's thickness. Having 92.5% transmission , assuming an atom velocity of 750m/s [1] and a square atom beam approximately $5mm$ per side indicates a flux of 3.422×10^{12} atoms per second.

While this flux is higher than that recorded in our previous tests, it is still not as high as we had anticipated. It is important to note that this last test was done without the cold "sleeves" in place, at a higher temperature than in my initial calculations, and most importantly without a precision aperture.

We originally tried using a piece of sheet metal with a hole drilled through it as

an aperture. but the hole was so small (about a 3mm diameter) that it was nearly impossible to align with the calcium beam and the laser beam. I decided to make the hole into a vertical slit (still about 5mm wide) so that it would be easier to intersect the laser with the atom-beam. I was able to do this because many simple experiments (including simple absorption measurements) do not rely on the vertical columnation of the atomic beam as much as the horizontal (direction of my laser) columnation. It was with this vertical slit that the previously reported data of 7.5% absorption was recorded.

2.2.3   Development of a Heated Aperture System

I designed an aperture system which both columnates the atomic beam and resists clogging. The device consists of one heated and one unheated aperture, both independently mounted. Using two apertures decreases the angular dispersion of the resulting atomic beam over using only one. By heating the initial opening, the atoms that do not pass cleanly through the aperture not collect on the edges of the opening and clog the aperture. It should be noted that this design has not yet been tested and these proposed outcomes are still theoretical.

As seen in Fig. 2.6, the new aperture system allows the experimenter to adjust the linear separation and radial alignment of the apertures. The system also allows the apertures themselves to be easily interchanged.

On both devices the aperture wafers are held into place by the cap screwing down onto the rotating mount. By making it simple to remove and replace the apertures, larger apertures can be used for faster and less demanding experiments (like observing Ramsey fringes), and smaller apertures can be used for more precise measurements (like an atomic time standard).

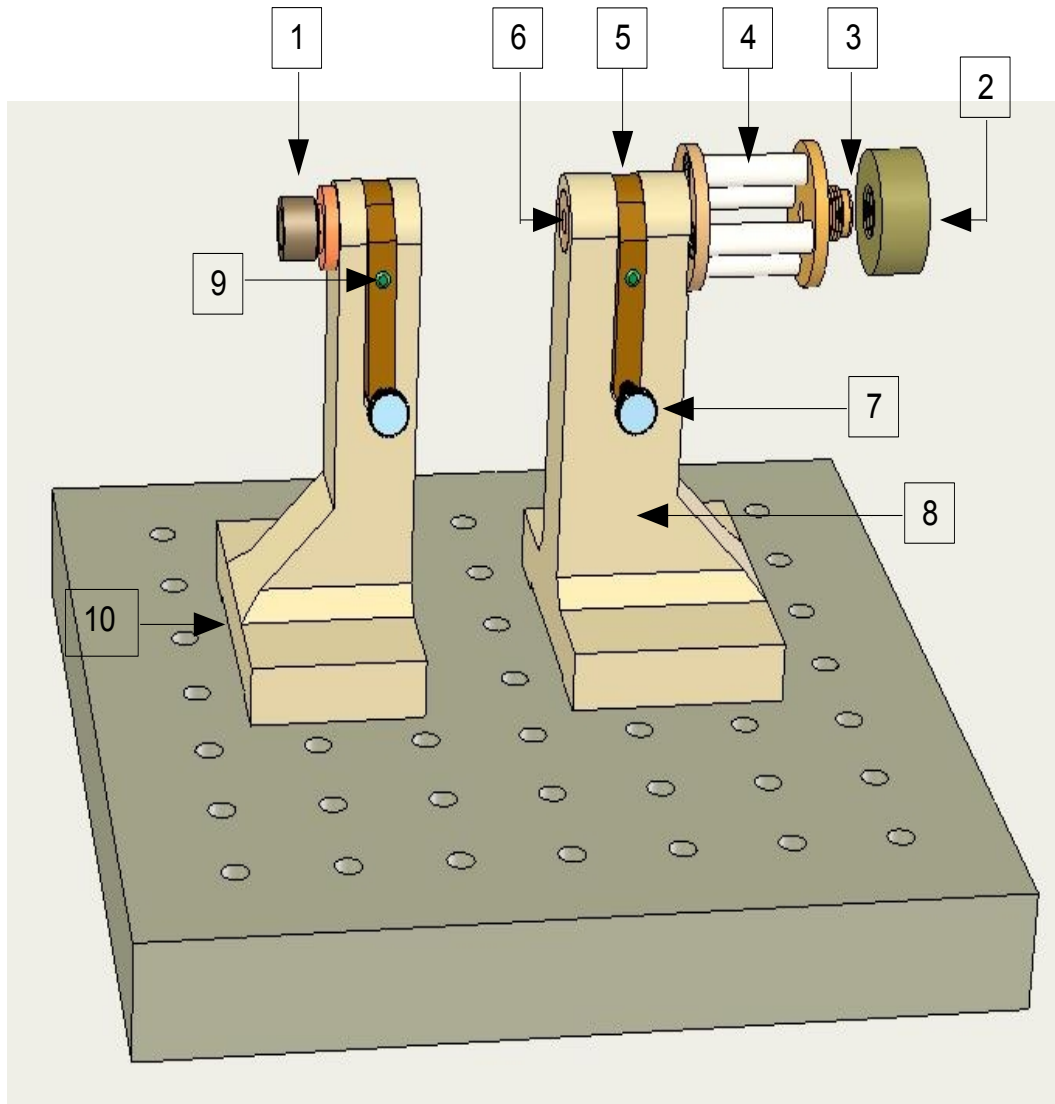The heated device has a larger screw-on cap which is wound and brazed with a

Figure 2.6 The new heated aperture system. (1) Unheated Cap. (2) Heated Cap. (3) Aperture Placement. (4) Ceramic Stand-offs. (5) Holding Fork. (6) Rotating Mount. (7) Fine Adjustment Tuning Knob. (8) Mount. (9) Set Screw. (10) "U-Shaped" Relief Cut

1mm wire heating element. The heating element has a maximum operating temperature of 1000°C and is thermally isolated from the rest of the experiment by four ceramic standoffs. The unheated device has a smaller screw-on cap.

Both devices use a holding fork with a set screw to hold the rotating mount in place. On the side of each fork is also a fine tuning adjustment knob, which allows precise angular positioning of the apertures. Each mount is held by a stand with a U-shaped "relief cut" in it's base. This cut ensures two points of contact between the base and the table, thereby giving guaranteed stability.

All pieces of this system will be made of stainless steel except for the ceramic stand-offs and the aluminum bases. I used only one metal for the majority of the device in order to avoid problems associated with thermal expansion between parts. As of the submission of this thesis, this aperture system was in the process of being built.

Chapter 3

Feasibility Calculations for a Proposed Ion Interferometer

3.1 Introduction

In classical electromagnetism the photon is assumed to have no rest mass. This assumption is necessary for many fundamental theories such as Gauss' Law and Coulomb's Law. However, it is yet to be proven that a photon has zero rest mass. What we do know is that if it does exist it is incredibly small – small enough that it has yet to be detected. Presented here is a discussion and study of the feasibility of a proposed table-top ion interferometer. This interferometer could detect a potential photon rest mass with greater sensitivity than previous lab experiments. If a non-zero rest mass is detected, there would be far reaching ramifications. For example, Maxwell's equations would need to be altered, there would be a longitudinal component to a photon's polarization, and there would be dispersion of light in vacuum.

   While true that classical electromagnetism forbids electrostatic fields inside empty

conducting shells, there is a possibility within quantum mechanics that minute fields may actually exist. Stemming from Yukawa's particle-exchange theory of forces [2], a modified version of Maxwell's equations was derived to account for a possible non-zero rest mass of the photon, the exchange particle of the Coulomb force [3]. Because a non-zero photon mass would limit the range of the Coulomb force, these modified equations violate Gauss' law and make non-zero electrostatic fields inside of the conductors possible.

3.1.1   Ion Interferometer Measurements

Progress on previous experiments searching for a photon rest mass has been slow - the limit of a non-zero photon rest mass, as determined by experiments, has decreased by only a factor of 2.5 over the past 35 years [4] [5]. My research group recently proposed to use ion interferometry to improve this measurement by *several orders of magnitude* [6]. In this experiment, a voltage would be applied across a concentric pair of conducting cylindrical shells. A beam of ions traveling through the inner shell would be split and recombined using either physical gratings or a laser. A non-zero electric field in the shell would induce a phase shift between the arms of the interferometer, resulting in a shift in the interference pattern.

Initial calculations were predicted assuming infinitely long cylinders, no fringing electric fields entering the cylinders, and no objects placed in the cylinders. In reality all three of these assumptions will be violated in a real device. I performed calculations of classical and non-classical electrostatic potentials in the proposed apparatus. I took all of these conditions into consideration to determine if the predicted sensitivity was valid and to verify that classical fringing fields would not limit the accuracy of the device. In this next sections of my thesis, I show the methods and results of these calculations.
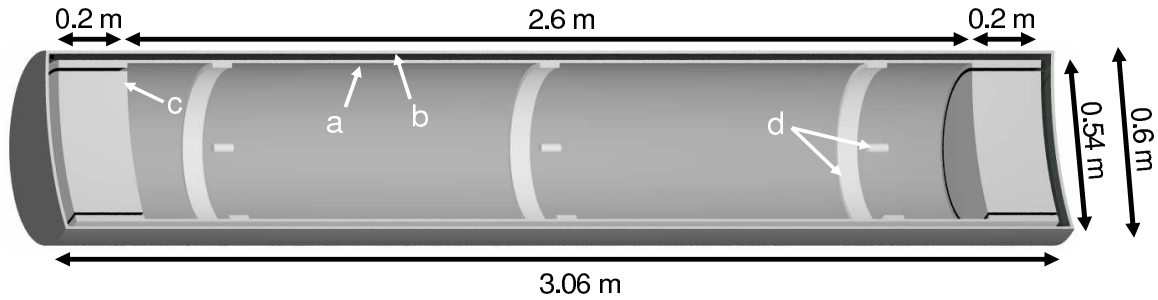
Figure 3.1 Layout of conductors. This scale figure gives a cut-away perspective view of the conductors which enforce the boundary conditions assumed in our calculations. Arrows point out (a) the inner conducting cylinder, (b) the outer conducting cylinder, (c) the disk which caps one end of the inner conductor, and (d) one of the three sets of additional conductors inserted into our calculation to explore the effect of mounting objects inside the inner conductor.

3.2 Calculations of Classical Fringing Fields

The first calculation I performed was for the classical fringing fields in concentric cylinders subject to the conditions I would expect in an actual physical experiment (see Fig.3.1). The cylinders were a definite length, fringing fields were allowed to enter through small holes in either end cap, and conducting objects attached to the cylinders were placed at various distances within the cylinders.

For the given set of static boundary conditions, the electric potential at any point within the cylinder can be found from Laplace's equation, which is Poisson's equation with the source set to zero. For reasons which will become apparent in the next section, the following derivation for classical field points is performed using Poisson's equation with the generic source term y:

$$\nabla^2 \phi_c = y. \tag{3.1}$$

However, it should be remembered that the source term was set to zero in the computer's code when performing the classical calculations.

For an axially symmetric system, Eq. 3.1 can be written as a two-dimensional

equation in cylindrical coordinates:

$$\frac{1}{r}\frac{\partial \phi_c}{\partial r} + \frac{\partial^2 \phi_c}{\partial r^2} + \frac{\partial^2 \phi_c}{\partial z^2} = y, \tag{3.2}$$

where r and z are the radial and axial coordinates.

I did my calculations using a finite difference method in which the potential is calculated at points on a grid. I approximated the derivatives to second order from adjacent points on the grid. The grid was evenly spaced in both dimensions by a distance a. The potential ϕ_c at each point on the grid will be written as $\phi_{i,j}$ where i and j are integers labeling the point.

I defined $i = j = 0$ at the center of the conducting shells, so that the actual coordinates of each grid point are equal to $r_i = ai$ and $z_j = aj$. With these definitions, Eq. 3.2 is approximated by

$$\frac{\phi_{i+1,j} - \phi_{i-1,j}}{2ar_i} + \frac{\phi_{i+1,j} - 2\phi_{i,j} + \phi_{i-1,j}}{a^2}$$
$$+ \frac{\phi_{i,j+1} - 2\phi_{i,j} + \phi_{i,j-1}}{a^2} = y_{i,j}. \tag{3.3}$$

This can be solved for $\phi_{i,j}$ in terms of the known quantity $y_{i,j}$ and the value of ϕ_c at adjacent grid points:

$$\phi_{i,j} = \frac{1}{4}\left[\left(1 + \frac{a}{2r_i}\right)\phi_{i+1,j} + \left(1 - \frac{a}{2r_i}\right)\phi_{i-1,j} \right.$$
$$\left. \phi_{i,j+1} + \phi_{i,j-1} - a^2 y_{i,j} \right]. \tag{3.4}$$

I started my simulation with an arbitrary value of $\phi_{i,j}$ at each grid point (usually zero). Then using Gauss-Seidel iteration [7], this equation was evaluated at each point to produce an updated value of $\phi_{i,j}$. After many iterations, $\phi_{i,j}$ eventually converged to the correct values to solve Eq. 3.3. To accelerate convergence, I used the successive over-relaxation method [7].

Special attention was given to the points at which $i = 0$. Since r is always positive in cylindrical coordinates, $\phi_{i,j}$ is not defined for negative values of i. But

there is effectively no difference between cylindrical and Cartesian coordinates for the row of points along the axis. So for these points I calculated derivatives using Cartesian coordinates knowing that the points directly below the axis and just into or out of the two-dimensional grid should have the same value as the point directly above each point on the axis. This gives the equation

$$\phi_{0,j} = \frac{1}{6} \left(4\phi_{1,j} + \phi_{0,j+1} + \phi_{0,j-1} \right). \tag{3.5}$$

In addition to exploiting axial symmetry and using successive over-relaxation, I also employed two other techniques to accelerate convergence. One took advantage of the conductors' mirrored symmetry about their center, which allowed me to throw away all points with $j < 0$, cutting the number of grid points in half. Doing this required me to treat the $j = 0$ points differently, because the grid no longer contained values for $\phi_{i,-1}$. By symmetry I knew that $\phi_{i,j} = \phi_{i,-j}$. This allowed me to replace $\phi_{i,-1}$ with $\phi_{i,1}$ in Eq. 3.4. The point $\phi_{0,0}$ is a special point, being both a member of the $r = 0$ and $z = 0$ subsets of points. For this point I used Eq. 3.5, but substituted $\phi_{0,1}$ for $\phi_{0,-1}$.

Another technique decreased computation time by successively reducing the size of the grid in the axial direction. This was done by finding columns which had already converged near their final value and then using these values as the new boundary conditions for a problem involving a smaller grid. To do this the program used a variable $jmax$, initialized to the largest j index on the grid, and only updated points with $j \leq jmax$. After each set of 100 iterations the program stopped and calculated the fractional error for each of the points with $j = jmax$. I defined fractional error to be

$$\left| \frac{\phi_{i,j} - \Phi_{i,j}}{\phi_{i,j}} \right|,$$

where $\phi_{i,j}$ is the actual value at grid point (i,j) and $\Phi_{i,j}$ is the value calculated from

Eq. 3.4 without actually changing any values on the grid.

If the fractional error at every point in this column was smaller than 10^{-8}, the program would reduce $jmax$ by one, thereby reducing the effective size of the grid. The program then repeated this process until it found a column which contained at least one point who's fractional error was larger than the specified value. If there were no points on the grid with a fractional error larger than 10^{-8}, the program terminated. Otherwise, the over-relaxation parameter was re-calculated and the next set of 100 iterations was performed.

The error introduced by this technique should be negligible. Supposing a column has converged to within a factor f of its final value, the error introduced into other points by "freezing" this column should be of the order f. Therefore, for a grid with N_x columns, the largest fractional error anywhere on the grid should be on the order of $f\sqrt{N_z}$ if the errors are assumed to be random, or smaller otherwise.

I employed these acceleration techniques while I was experimenting with different geometries and setups in order to speed up computation time. However, since I haven't done a rigorous study of this method, once I had run the simulations many times, felt confident with the results, and had decided on a definite geometry, I ran the simulation without this "stepping in" short-cut to verify my data. The result of these calculations were identical to those done with the "stepping in" technique up to the seven digits of precision saved at the end of the calculations.

3.3   Calculations of Non-Classical Potentials

For the non-classical fields inside the cylinders, the mathematical formula for ϕ was not as straight forward as simply using Laplace's equation. However, after some approximations and manipulations we are left with a formula for ϕ invoking only

Poisson's equation.

We start with the massive-photon counter-part of Laplace's equation

$$\nabla^2 \phi - \mu^2 \phi = 0 \tag{3.6}$$

where μ is proportional to a photon mass m_γ by $\mu = m_\gamma c / \hbar$. To simplify calculations, instead of solving for ϕ directly in the non-classical fields, we solved for the deviation from the classical $\phi_p = \phi - \phi_c$, making Eq. 3.6

$$\nabla^2 \phi_c + \nabla^2 \phi_p - \mu^2 \phi_c - \mu^2 \phi_p = 0. \tag{3.7}$$

Now we take into consideration that $\nabla^2 \phi_c = 0$. Also, since μ is expected to be very small, ϕ_p will be small in comparison to ϕ_c and gives reasonable grounds to drop the last term. It is not immediately clear what μ equals, so we can normalize our equation with a new parameter $\phi_s = \phi_p / \mu^2$, thus leaving us with

$$\nabla^2 \phi_s = \phi_c. \tag{3.8}$$

Again this is simply Poisson's equation, this time with the source term $y = \phi_c$. Therefore my simulation (for both classical and non-classical fields) only needed to solve equations of the form

$$\nabla^2 \phi_x = y. \tag{3.9}$$

To calculate the non-classical field, I substituted the classical field points I computed in section 3.2 as source terms in Eq. 3.8. From this point I employed the same computational techniques in solving for the non-classical fields as I did for the classical fields.

3.4   Results

For the classical fringing-field calculation I was mainly interested in how the potential inside the inner conductor varies from the voltage (V) of the inner conductor. To keep

round-off error from completely hiding these variations, I made use of the fact that classical electromagnetism allows me to arbitrarily add a constant potential. So rather than solving Laplace's equation for ϕ_c, I instead solved for $\Delta\phi_c = \phi_c - V$ using the same equation but different boundary conditions — $-V$ on the outer conductor and 0 on the inner conductor. This way I found deviations from zero rather than from some finite potential. The results of these calculations are shown in Fig.3.2 (a).

To verify these results, a fellow member of my group used a series solution to approximate the field inside of the inner conductor assuming a much more simple geometry and that the inner conductor was grounded. Though a rough approximation, this calculation showed that the potential at the center of the tube would be about 4.5×10^{-7} times the potential inside the radial slices, in good agreement with my numerical calculation. He also found a series solution for the field between two grounded cylinders with a fixed potential applied to the gap at the ends. The field in the center of the gap turned out to be 2×10^{27} times smaller than the potential at the end, also in agreement with my numerical calculation.

For the non-classical potentials, it is important to remember that ϕ_s is the deviation from the classical field, not the actual non-classical potential. As such, the boundary conditions were that $\phi_s = 0$ at each of the conductors.

Since I made the boundaries 0 on the outer conductor and $-V$ on the inner conductor for the classical calculations, I had to add V to ϕ_c to get the actual potential needed for the non-classical equation's source term. However, because I used a double-precision floating-point format, this addition caused substantial inaccuracies in the region between the conductors. Fortunately I was only interested in the area within the inner conductor, which should not be affected by this lost precision — the non-classical potential is predominantly generated by the local source term y rather than from fringing fields generated outside the inner conductor. To be extra careful, we
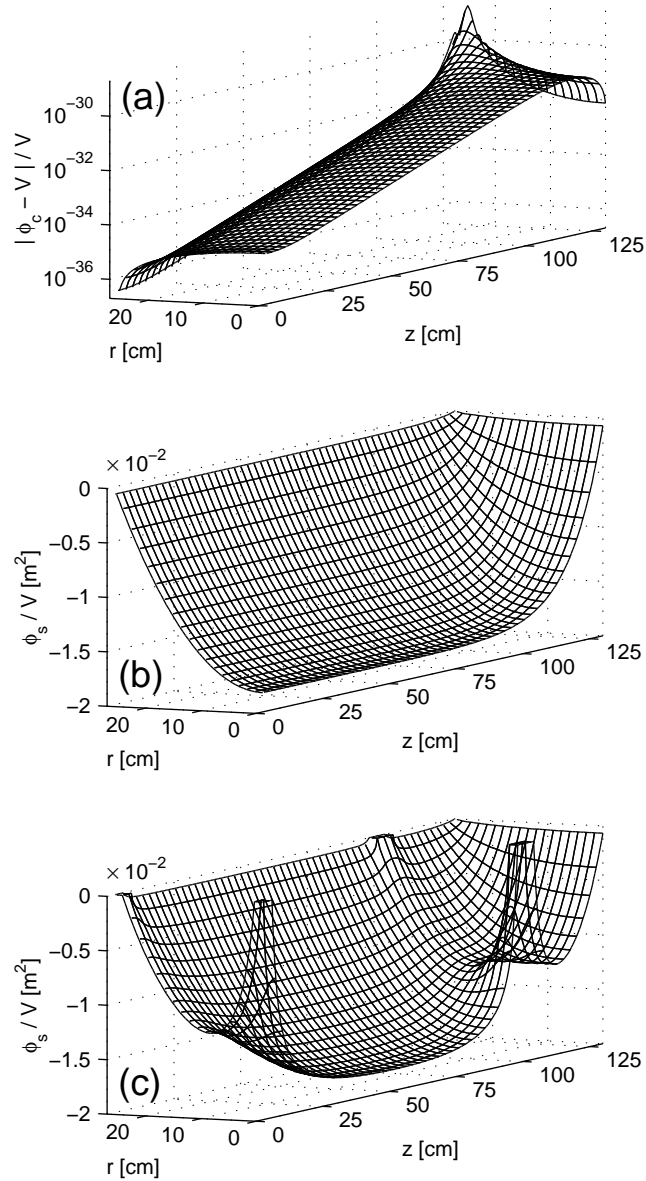
Figure 3.2

The results of the numerical calculations. All calculations were done with a grid spacing of $a = 1.67 \times 10^{-2}$ cm. Only the region inside the inner conductor is shown. In (a) a semi-log plot of the classical fringing-field potential is shown. The peak in the upper right-hand corner is at the location of the radial slice in the end cap. In (b) the non-classical potential ϕ_s is plotted. Frame (c) shows the effect of additional conducting objects inside the inner shell. Note — due to symmetry, each plot shows only half of the field.

also calculated ϕ_c directly using the correct boundary conditions and used these values whenever ϕ_c was less than $\frac{V}{2}$.

The results of this calculation are shown in Fig.3.2 (b). Figure 3.2 (c) shows the results of a similar calculation in which additional conductors were added to simulate optics and other objects inside the inner shell. These conductors consisted of a ring and a cylinder at the three locations where gratings would be positioned in the interferometer. The rings were assumed to be 6 cm wide and 1.5 cm thick, just touching the inner shell, and the cylinders to be 6 cm long and 1.5 cm in radius, centered on the axis of the inner shell, as shown in Fig 3.1. These conductors were assumed to be at the same potential as the inner shell.

I would estimate the error in these calculation to be very small — to the seven digits output by our program there was no change in ϕ_s when we increased the grid spacing by a factor of 3.

3.5   Discussion

The fields are compared in Fig. 3.3. While this figure shows the *potential* at *each point* moving radially from the axis, for the proposed ion interferometer experiment, all that is important is the *field at the location of the ion beam*. As such, the most important information in this figure is the radial slope of the potential at $r = 25$ cm.

In Fig. 3.3 (a) we see that the non-classical field is approximated very well by the field of an infinite cylinder. In Fig. 3.3 (b) we see that although the effect of small objects inside the shell on the non-classical potential is not negligible, it should not greatly change the sensitivity of the experiment as long as care is taken. Because of the axial symmetry of our setup, we modeled rings instead of rectangles (which would better approximate an optical mount) in the calculations as additional conductors
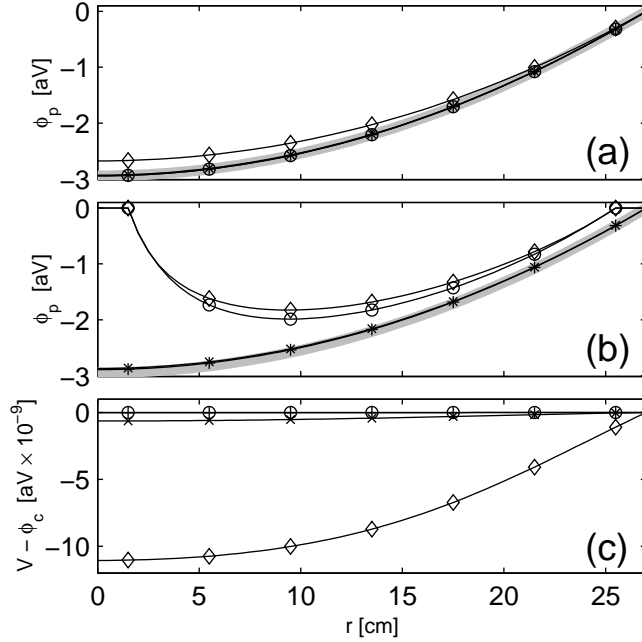
Figure 3.3 Comparing the different potentials. The potential is plotted as a function of radius at four different points along the axis. In (a) the non-classical field is shown. In (b) the non-classical field is shown for the case in which additional conductors have been placed inside the inner shell. In (c) the classical field is shown. The lines marked with circles and diamonds are at axial distances of 0 and 100 cm from the center of the conductors — the locations of the gratings. The lines marked with + and × are at axial distances of 33 and 67 cm, respectively. All potentials were plotted assuming that $V = 200 \, \text{kV}$ and $\mu = 2.8 \times 10^{-11} \, \text{m}^{-1}$. The thick grey lines in (a) and (b) represent the analytical solution for the non-classical field inside of an infinite cylinder.

inside the cylinders, thereby making this plot an extreme "worst-case" estimate.

It should be noted that the vertical axis in Fig. 3.3 (c) is about 2.4×10^8 times smaller than in (a) and (b), indicating that the fringing-fields inside the inner conductor should be completely negligible for values of μ much smaller than 2.8×10^{-11} m^{-1} (corresponding to a photon rest mass of 1×10^{-53} kg, over 600 times smaller than the current experimental limit measured in [5]). Consequently, fringing fields should not be a problem in the proposed experiment.

Bibliography

[1] N. F. Ramsey, Proceedings of the International School of Physics. **6**, (1992).

[2] H. Yukawa, in *Nobel Lectures, Physics 1942-1962* (Elsevier, 1964).

[3] J. D. Jackson, *Classical Electrodynamics* (Wiley, New York, 1975), 2nd ed.

[4] E. R. Williams, J. E. Faller, and H. A. Hill, Phys. Rev. Lett. **26**, 721 (1971).

[5] R. E. Crandall, Am. J. Phys. **51**, 698 (1983).

[6] B. Neyenhuis, D. Christensen, and D. S. Durfee, ArXiv:physics/0606262 (2006).

[7] W. H. Press, S. A. Teukolsky, W. T. Vetterling, and B. P. Flannery, Numerical Recipes in C: The Art of Scientific Computing, 2nd Edition, Cambridge University Press, Cambridge (1992), pp. 827-888. http://www.nrbook.com/a/bookcpdf.php